Time-Resolved SAXS Studies of a Sphere-Forming Block Copolymer under Large Oscillatory Shear Deformation

Gakuji Shin,[†] Naoki Sakamoto,[‡] Kenji Saijo, Shoji Suehiro,[§] and Takeji Hashimoto*

Department of Polymer Chemistry, Graduate School of Engineering, Kyoto University, Kyoto 606-8501, Japan

Kazuki Ito

Institute of Applied Biochemistry, The University of Tsukuba, Tsukuba 305-3587, Japan

Yoshiyuki Amemiya

Division of Transdisciplinary Sciences, Department of Advanced Materials Science, Graduate School of Frontier Sciences, University of Tokyo, Tokyo 113-8656, Japan

Received February 7, 2000; Revised Manuscript Received August 11, 2000

ABSTRACT: The deformation mechanism of polystyrene-*block*-poly(ethylene-*alt*-propylene) diblock copolymer having soft spherical microdomains composed of poly(ethylene-*alt*-propylene) block chains in a hard matrix composed of polystyrene block chains under large oscillatory shear deformation with a strain amplitude of 0.41 at an angular frequency of 0.0944 rad s^{-1} was investigated by the synchrotron radiation dynamic small-angle X-ray scattering (SR-DSAXS) method at temperatures of 95 and 158 °C. The 2D SAXS pattern was detected with an imaging plate (IP) simultaneously with stress measurement on specimens with the purpose to elucidate a relationship between macroscopic properties of the system as revealed by rheological measurements and response of its mesoscopic structure to the applied deformation as revealed by SAXS measurements. The SAXS result indicated that the spheres are packed in a body-centered-cubic (bcc) lattice with a paracrystal distortion. The local strain amplitude actually imposed on the spherical microdomains (γ_{sphere}) and that on the {110} lattice spacing (γ_{lattice}) were measured as a function of strain phase, strain cycle N at the two temperatures. Both γ_{sphere} and γ_{lattice} at each temperature decay with N, in parallel to the stress decay with N. The decays of γ_{sphere} and γ_{lattice} with N at 158 °C are larger than those at 95 °C. At a given temperature the decay of γ_{lattice} is larger than that of γ_{sphere}. The Lissajous pattern of shear stress versus shear strain obtained in the first cycle showed almost a linear stress response to the strain. However, the nonlinearity develops and increases with N, and this nonlinearity is larger at 158 °C than at 95 °C. The shear deformation under this experimental condition did not induce a strong preferential lattice orientation: The lattice orientation remain essentially unaltered with N.

1. Introduction

Block copolymers exhibit a wide variety of ordered microdomain structures with a nanometer scale periodicity. The dynamic response of such microdomain structures in block copolymers to an applied stress or strain field provides fascinating research topics on open nonequilibrium systems. A pioneering study of a flow effect on such ordered microdomain structure was first performed by Keller et al.[1] using an extruding process. In their work, they prepared highly aligned hexagonally packed cylindrical microdomains from polystyrene-*block*-polybutadiene-*block*-polystyrene (SBS) triblock copolymer melts. Hadziioannou et al.[2] produced highly aligned hexagonally packed cylinders and lamellae from polystyrene-*block*-polyisoprene-*block*-polystyrene (SIS) triblock and polystyrene-*block*-polyisoprene (SI) diblock copolymer melts using a large-amplitude oscillatory shear strain (LAOS). Since then, numerous attempts have been made by many researchers to study the shear-induced alignment of the ordered structures in block copolymer melts using TEM (transmission electron microscopy), SAXS (small-angle X-ray scattering), SANS (small-angle neutron scattering), and birefringence. In recent years, many experimental reports have been published on the shear-induced orientation of lamellar,[3−9] cylidrical,[10−13] and spherical microdomains.[14−16] The shear effects on disorder-to-order transition[17,18] and order-to-order transition[19−22] are also discussed.

In this paper we are concerned with a block copolymer containing spherical microdomains. The deformation mechanism of the spherical microdomains was previously reported by Almdal et al.,[14] Phoon et al.,[15] and Okamoto et al.[16]

Almdal et al.[14] explored the effects of LAOS (strain amplitude 1.0 with $\omega = 0.02$ rad s^{-1}) on the orientation of spheres packed in a body-centered-cubic (bcc) lattice in the poly(ethylenepropylene)-*block*-poly(ethylethylene) (PEP−PEE) diblock copolymers. They studied the shear effect at temperatures 70−90 °C, relatively close to the order−disorder transition temperature, $T_{\text{ODT}} = 105 \pm 5$ °C. In the temperature range studied, both the matrix and the spherical domains are far above their glass transition temperatures, and both phase have similar stiffness. Their results indicated that the shear strain

---

* To whom correspondence should be addressed.

[†] Present address: Specialty Polymers Laboratories, Mitsubishi Chemical Corporation, 1 Toho-cho, Yokkaichi, Mie 510-8530, Japan.

[‡] Present address: R & D Administration, Asahi Chemical Industry Co., Ltd., 1-1-2 Yuraku-cho, Chiyoda-ku, Tokyo 100-8440, Japan.

[§] Present address: Department of Apparel Arts, Kurashiki City College, 160 Hieda-cho, Kojima, Kurashiki, 711-0937, Japan.

10.1021/ma000226m CCC: $19.00

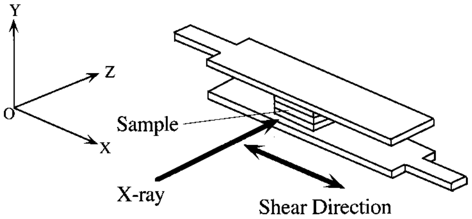

Figure 1. Laboratory coordinate system for DSAXS experiment. The Cartesian coordinate *OXYZ* is defined such that the *Z*-axis is parallel to the incident X-ray beam and the *Y*-axis is parallel to shear gradient direction and the *X*-axis is parallel to shear direction. An oscillatory shear deformation with a frequency of 0.0944 rad s^{-1} is imposed.

induced a preferential orientation of (110) lattice planes parallel to the *XZ*-plane and ⟨111⟩ direction parallel to the *X*-axis. The definition of the laboratory coordinate system will be given in Figure 1. Here the *X*-axis is parallel to the deformation of the sample, and the *Y*-axis is parallel to the velocity gradient.

Okamoto et al.[16] studied the shear effect on the deformation of the bcc lattice formed by hard spherical microdomains composed of polystyrene block chains (PS) in a soft matrix composed of poly(ethylene-*alt*-propylene) block chains (PEP) with LAOS (strain amplitude 0.50 with $\omega = 0.0936$ rad s^{-1}) at temperature $T = 25$ °C. Their system is far below the T_{ODT}, which is estimated to be 180 ± 5 °C by SAXS, and PS spheres are vitrified in the molten matrix of PEP. Their results indicated that the shear deformation induced a preferential orientation of (110) lattice planes parallel to the *XZ*-plane and the ⟨110⟩ direction parallel to the *OY* direction and that the deformation of the bcc lattice under this particular (110) lattice plane orientation occurred nearly in phase to the applied strain. They found the orientation was completely relaxed after cessation of the shear, contrary to the results reported by Almdal et al.[14]

To investigate the effect of the composition of the block copolymer to the deformation behavior, in this work we conducted dynamic SAXS measurements using a diblock copolymer having a composition and hence a structure complementary to the diblock copolymer studied by Okamoto et al.;[16] i.e., the structure we shall investigate here is composed of relatively soft spherical microdomains composed of PEP block chains packed in a bcc lattice with a paracrystal distortion[23,24] in a relatively hard matrix composed of PS. We studied here the shear effect at a frequency $\omega = 0.0944$ rad s^{-1} and at temperature $T = 95$ and 158 °C; the frequency was close to that used by Okamoto et al.,[16] and the temperatures were much far below T_{ODT}, which is too high to be measured, but both the matrix phase and the sphere phase are above their glass transitional temperatures (T_g's), though the $T = 95$ °C is only slightly higher than the T_g of the PS matrix of the block copolymer used in this study (determined to be ~88 °C by using DSC). Here we report some initial results of our studies.

2. Experimental Section

2.1. Specimen. The sample studied here is a polystyrene-*block*-poly(ethylene-*alt*-propylene) copolymer (SEP) which was kindly supplied from Kuraray Co., Ltd., Japan. It was prepared by selective hydrogenation of a polyisoprene block of a precursor SI diblock copolymer prepared by living anionic polymerization. It has a number-average molecular weight $M_n = 1.06 \times 10^5$ and heterogeneity index $M_w/M_n = 1.26$, where M_w is weight-average molecular weight. The volume fraction of PS blocks in the copolymer is 0.90. The as-received sample was prepared by first dissolving a predetermined amount of SEP (10 wt %) in toluene and then slowly evaporating the solvent at room temperature for 1 week.

The film specimens of the SEP used here had a microdomain structure composed of spherical microdomains of PEP blocks on a cubic lattice dispersed in the matrix of PS blocks. The determination of a type of cubic lattice which exists in our sample is very important for the discussions throughout this work. For this purpose we employed both a volume analysis and a paracrystal analysis. Both analyses favored a body-centered-cubic lattice (bcc) rather than a simple cubic lattice (sc) and face-centered-cubic lattice (fcc). The paracrystal analysis compared the experimental SAXS profile with the theoretical profile calculated from the three types of cubic lattices with paracrystal distortions.[24] The result revealed that the system has the bcc structure with considerable paracrystal lattice distortions. The volume analysis compares the stoichiometric volume of PEP ($f_{\mathrm{stoi}} = 0.10$) estimated from molecular weight and composition of the SEP with the volume of PEP spheres (f_{SAXS}) estimated by SAXS profile,[25] both based upon a complete segregation of the PEP and PS blocks into the corresponding phases. f_{SAXS} was estimated to be 0.16, 0.11, and 0.12 for sc, bcc, and fcc, respectively. Although the f_{SAXS} values for both bcc and fcc give a close agreement with f_{stoi}, bcc is slightly favored over fcc.

The weight-average molecular weights of the PEP block and the PS block are larger than the reported molecular weights between entanglement couplings of the corresponding homopolymers ($M_{\mathrm{e,PEP}} \cong 1660$[26] and $M_{\mathrm{e,PS}} \cong 18\,100$[27]) by a factor of ~6.6 and ~6.8, respectively. Thus, the PEP block in the PEP spheres and the PS blocks in the PS matrix are expected to be entangled, although $M_{\mathrm{e,PEP}}$ and $M_{\mathrm{e,PS}}$ in the microdomain space (confined space) may be different from those in the corresponding homopolymer space (or free space).

DSC measurements were performed with a Perkin-Elmer DSC7. The specimen in the cell was first heated to 150 °C and annealed at this temperature for 1 h and then followed by a slow cooling at 0.1 °C/min to 50 °C. The DSC thermogram was then taken during heating the specimen at 20 °C/min. The thermogram indicated onset of the deviation from the linear relationship in heat flow vs temperature at ~87.5 °C. We assigned T_g for the PS matrix to be ~88 °C.

2.2. Rheooptical Measurement. Simultaneous SAXS and stress measurements were performed by the synchrotron radiation dynamic small-angle X-ray scattering (SR-DSAXS) apparatus at beamline 15A of the Photon Factory, Institute of Materials Structure Science, High Energy Accelerator Research Organization, Tsukuba, Japan. Beamline 15A has demagnifying mirror−monochromator optics. The wavelength (λ) of incident X-ray was 0.15 nm, and the spectral distribution was $\Delta\lambda/\lambda = 10^{-3}$.

Figure 1 shows a layout of the sample deformation device. The DSAXS system comprises a stage-mounted imaging plate (IP) system developed at the Photon Factory and a hydraulic sample deformation device developed at Kyoto University. The stress and the strain of the sample are measured simultaneously with the SAXS data acquisition in order to correlate the deformation of the internal structure with the mechanical properties of the sample. Details of the DSAXS system are described elsewhere.[28−31]

Six to seven sheets of as-cast films of sizes ca. 7 mm along *X*-axis by 5 mm along *Z*-axis are stacked to make the total thickness to be ca. 3 mm along *Y*-axis and are sandwiched between two metal plates, and the oscillatory shear strain was imposed on the specimen by moving one of the metal plates parallel to the other. The Cartesian coordinate *OXYZ* used in this work is defined such that the *X*-axis is parallel to the shear direction and *Y*-axis is parallel to the velocity gradient, as shown Figure 1. The incident X-ray beam was along the *Z*-axis, and the beam spot size at the sample was ~1.5 mm^2. The SAXS intensity distribution was detected with an IP. The sample-to-detector distance was 1.6 m.

The amplitude γ_0 and the angular frequency ω of the sinusoidal shear strain were 0.41 and 0.0944 rad s^{-1}, respectively. Measurements were carried out at temperatures of 95 and 158 °C. The frequency selected in this study is lower than those sensitive to local dynamics of block copolymer chains in the respective micodomains, but it is rather sensitive to low-frequency dynamics (e.g., brush-on-brush disentanglement regimes,[32] see Figures 4 and 5). The stacked films were annealed at temperatures where the experiments were conducted so that they were well welded each other under the experimental conditions employed in this study. We did not find any pieces of evidence showing slippage occurring between the macroscopic layers of the stacked films.

2.3. Mechanical Measurement. Dynamic mechanical properties of specimens were measured with a Rheometrics Mechanical spectrometer (model RMS 800, Rheometrics Co., Ltd) using cone plate fixtures (8 mm diameter). Dynamic frequency sweep experiments were conducted, and the real and imaginary parts of dynamic shear moduli G' and G'' were measured as a function of angular frequency (ω) ranging from 0.01 to 100 rad s^{-1} at same temperatures as rheooptical experiments, namely 95 and 158 °C.

3. Experimental Results

3.1. Characterization of the Undeformed State. Figure 2 shows 2D SAXS pattern taken with an IP (part a) and the sector-averaged SAXS intensity distribution, $I(q,\mu=0°)$ (part b) and $I(q,\mu=90°)$ (part c) at 95 °C before applying oscillatory shear, where q is the scattering vector defined by $q = (4\pi/\lambda)\,\sin(\theta/2)$, θ being the scattering angle, and the sector width in the sector-average calculation was 10°. The azimuthal angle μ is defined as shown in Figure 2a; i.e., $\mu = 0°$ and $\mu = 90°$ correspond to the OX and the OY direction, respectively. As seen in Figure 2a and also by comparing the two profiles in parts b and c of Figure 2, the scattering pattern was somewhat deformed, indicating that the sample underwent uniaxial compression to some extent, being pressurized between the two parallel plates in the process to obtain good contact to the plates.

In Figure 2a the inner two arrows indicate the first-order scattering maximum from {110} lattice planes (i.e., (110) and $(\bar{1}10)$ lattice planes) and the second-order maximum from {200} lattice planes (i.e., (200) and $(\bar{2}00)$ lattice planes) of the bcc lattice, located at $q \cong q_m$ and $\sqrt{2}q_m$, respectively. On the other hand, the outer arrow indicates the broad scattering maximum located at $q \cong q_{m,p}$ arising from the form factor of isolated spheres. It should be noted, however, that the bcc lattice should have a considerable distortion as evident from the SAXS profiles exhibiting only up to the third-order scattering maxima from the lattice (located at q_m, $\sqrt{2}q_m$, and $\sqrt{3}q_m$) in Figure 2a,b.[24] A close observation of the 2D diffraction patterns from the {110} and {200} lattice planes along azimuthal angle μ may disclose a modulation of their diffraction intensities with μ. Thus, both the {110} and {200} diffraction patterns appear to be composed of eight diffraction spots (two spots each along $\mu = 0°$, 45°, 90°, and 135° at strain phase $\phi = 0°$, for example), though they are substantially overlapped, and the splitting of the spots is not necessarily very obvious. This indicates that the bcc lattice may have two kinds of preferential orientations as illustrated in Figure 2d: one with (110) planes parallel to XZ-plane and the other with (200) parallel to XZ-plane. This type of preferential orientation was considered to be built up as an initial condition in the process of sandwiching and welding the stack of the film specimens between the parallel plates (see Figure 1).

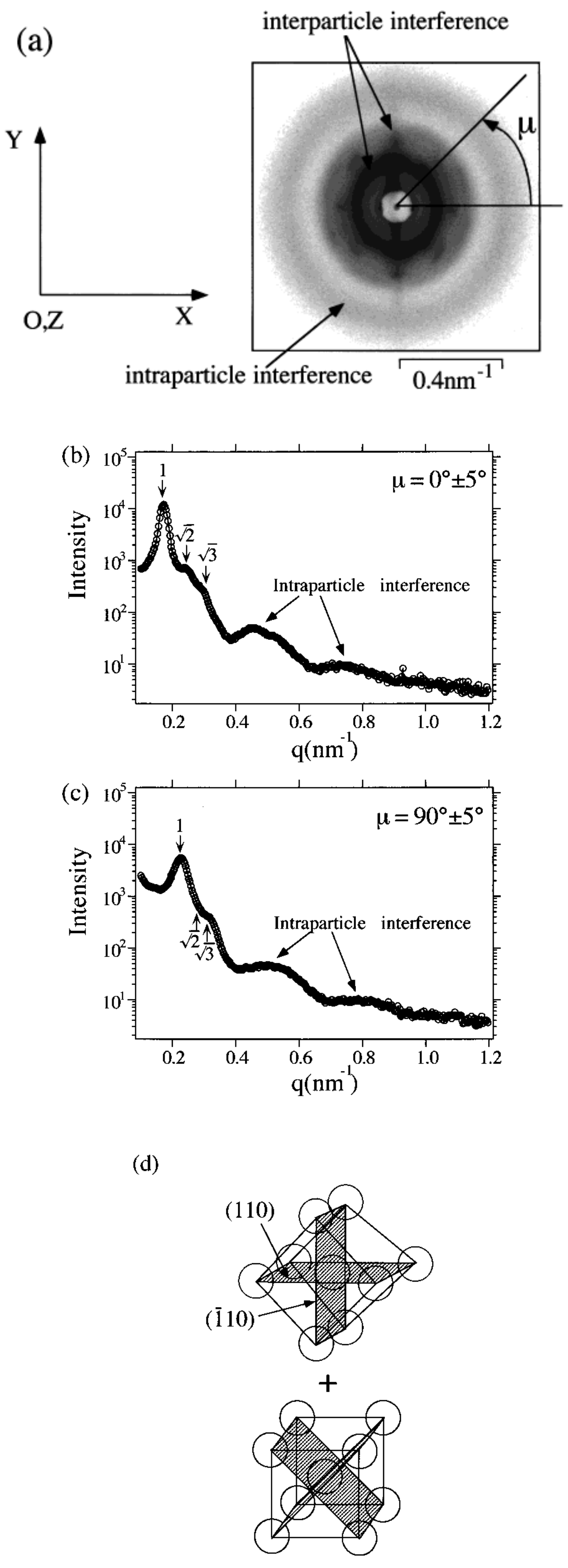

Figure 2. (a) 2D SAXS pattern taken with an IP and the sector-averaged SAXS intensity distribution with respect to q: (b) from the azimuthal angle $\mu = -5°$ to 5°and (c) from $\mu =$ 85° to 95°, at 95 °C for the undeformed SEP copolymer. (d) A model showing the mixture of preferred (110) and (200) orientations, both parallel to the XZ-plane.

As seen in Figure 2b, $I(q)$ along the OX direction, $I(q,\mu=0°)$, shows the sharp first-order maximum at $q_{m,OX} = 0.17$ nm^{-1} and shoulders at $\sqrt{2}q_{m,OX}$ and $\sqrt{3}q_{m,OX}$ and another maximum at $q_{m,p} = 0.48$ nm^{-1} which is designated as $q_{m,p,OX}$ hereafter. According to Figure 2c, $I(q)$ along the OY direction, $I(q,\mu=90°)$, also shows peaks

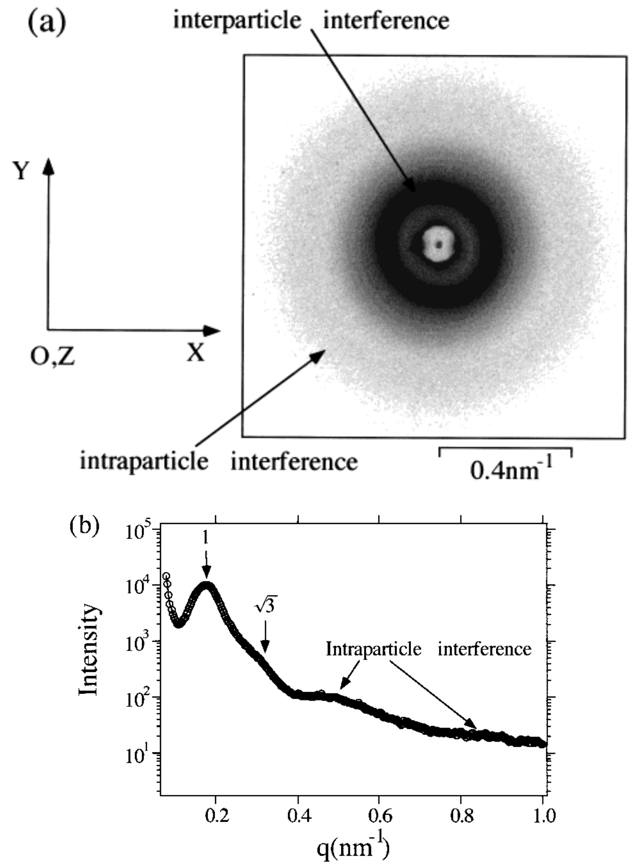

Figure 3. (a) SAXS pattern taken with the 2D detector for the undeformed SEP copolymer at 158 °C. (b) The sector-averaged SAXS intensity distribution over the azimuthal angle $\mu = -5°$ to 5°, plotted with scattering vector q.

similar to $I(q,\mu=0°)$, but the peak positions of $I(q,\mu=90°)$ are at somewhat wider angles than those of $I(q,\mu=0°)$. $I(q,\mu=90°)$shows the first-order maximum at $q_{\mathrm{m},OY} = 0.24\ \mathrm{nm}^{-1}$ and shoulders at $\sqrt{2}q_{\mathrm{m},OY}$ and $\sqrt{3}q_{\mathrm{m},OY}$ and another maximum at $q_{\mathrm{m,p}} = 0.50\ \mathrm{nm}^{-1}$, which is designated as $q_{\mathrm{m,p},OY}$. The close analyses of $I(q,\mu)$ (along with the TEM observation) yield the following pieces of information: (i) soft spherical PEP microdomains are dispersed in the matrix of hard PS block chains, (ii) the first-order maximum and the higher-order shoulders reflect the intersphere interference of the scattered waves, reflecting the diffractions from {110} and {200} lattice planes, while the maximum at $q_{\mathrm{m,p}}$ reflects the form factor of isolated spheres, and (iii) the average radius of the spheres along OX direction R_{OX} was calculated as 12.0 nm from $q_{\mathrm{m,p},OX}$, whereas the average radius along OY direction R_{OY} was calculated as 11.5 nm from $q_{\mathrm{m,p},OY}$.[33] Thus, the aspect ratio of the spheroids, i.e., the uniaxially compressed spheres, was determined as 0.958.

Figure 3 shows 2D SAXS pattern at 158 °C (part a) and sector-averaged SAXS intensity distribution, $I(q,\mu=0°)$ (part b), before shear. In Figure 3a the inner arrow indicates the first-order scattering maximum from {110} lattice planes, while the outer arrow indicates the broad scattering maximum arising from the form factor of isolated spheres. The first-order maximum at 158 °C is much broader than that at 95 °C, indicating that the lattice distortions at 158 °C are much greater than those at 95 °C. The maximum has no azimuthal angle dependence so that the weak lattice orientation which existed at 95 °C was completely relaxed at 158 °C. The radius of spheres and the Bragg spacing at 158 °C were calculated as 13.7 and 34.9 nm, respectively, from $q_{\mathrm{m,p}} = 0.42\ \mathrm{nm}^{-1}$ and $q_{\mathrm{m}} = 0.18\ \mathrm{nm}^{-1}$.

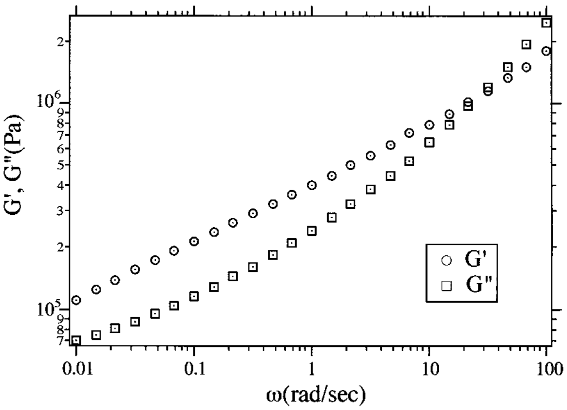

Figure 4. Linear dynamic mechanical properties at 95 °C. G' and G'' are the real and imaginary parts of the shear moduli, respectively.

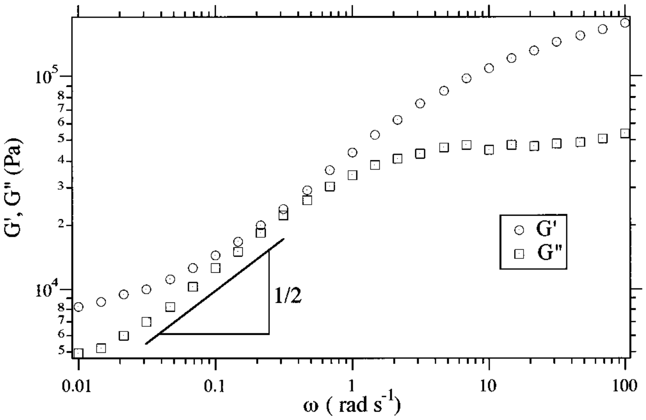

Figure 5. Linear dynamic mechanical properties at 158 °C. G' and G'' are the real and imaginary parts of the shear moduli, respectively.

3.2. Mechanical Properties. Figures 4 and 5 show the linear dynamic mechanical response with dynamic strain amplitude 1% and static strain 0% measured at 95 and 158 °C, respectively, where real and imaginary parts of the shear moduli, G' and G'', were plotted against ω in a double-logarithmic scale. The power-law behaviors of G' and G'' at the low-frequency limit are typical of the block copolymer melts having ordered microdomains.

Figures 6a and 7a show the shear stress and the shear strain plotted against time which were detected simultaneously with SAXS data under LAOS at 95 and 158 °C, respectively. At both temperatures the stress decayed as a function of N. Nonlinear stress response is remarkable in the 40th cycle at 158 °C. The mechanical response under LAOS at 158 °C obviously shows a greater viscous dissipation process compared with that at 95 °C, as will be evident from the fact that a phase lag of strain against stress at 158 °C is larger than that at 95 °C. This trend is consistent with that shown in Figures 4 and 5 for the linear viscoelastic behavior at $\omega = 0.0944\ \mathrm{rad\ s}^{-1}$.

Lissajous figures of shear stress versus shear strain in (b) the 1st, (c) the 5th, and (d) the 40th cycles, at temperatures 95 and 158 °C, are plotted in Figure 6b–d and Figure 7b–d, respectively. At 95 °C the Lissajous

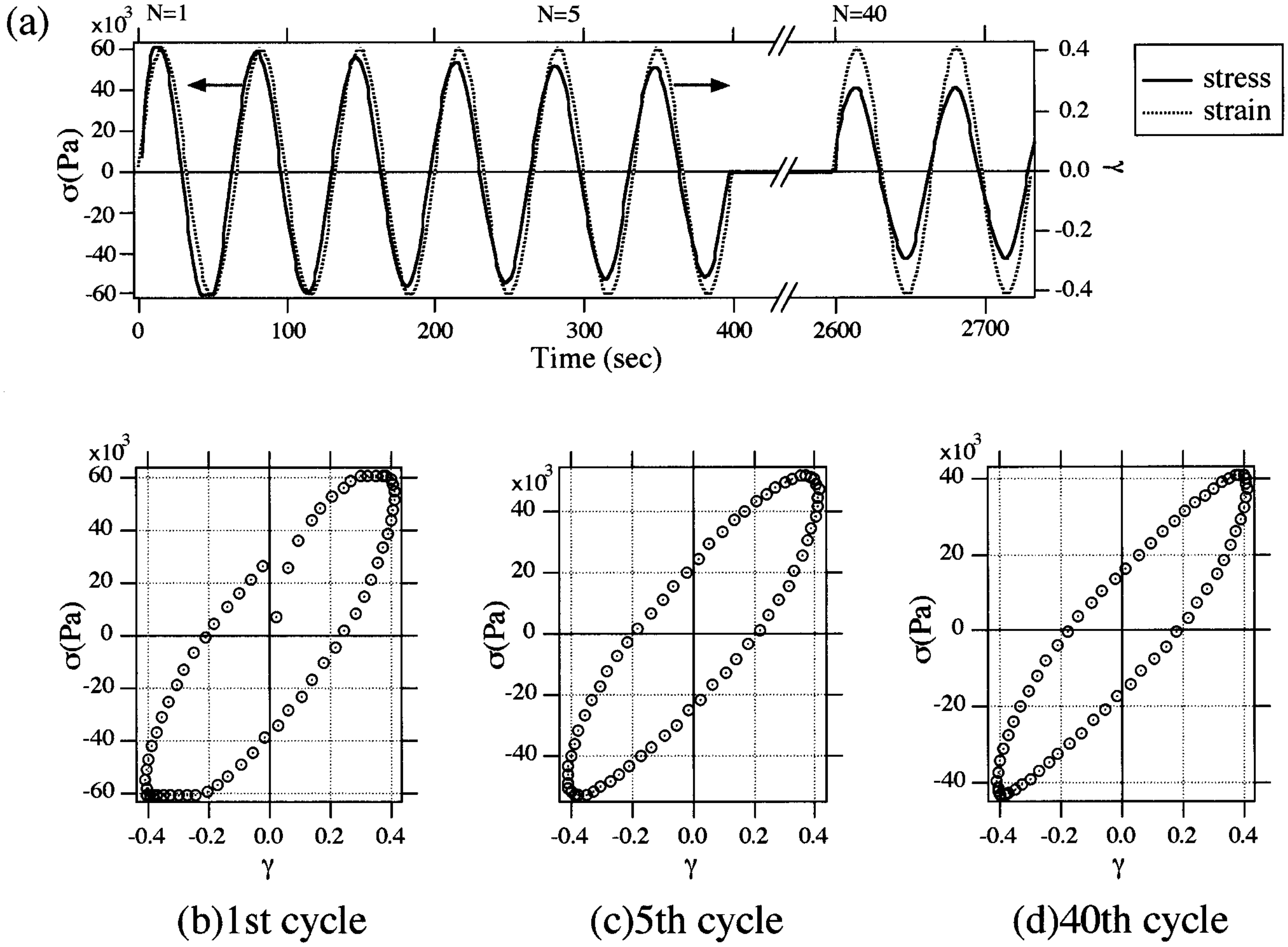

(b)1st cycle (c)5th cycle (d)40th cycle

Figure 6. Shear stress and shear strain against time detected simultaneously with the SAXS data at 95 °C (a). The Lissajous figures of shear stress versus shear strain obtained at the 1st (b), the 5th (c), and the 40th cycles (d).

figures show a relatively linear response at all cycles. On the other hand, at 158 °C, the relatively linear stress response as seen in the first cycle becomes nonlinear with increasing the number of strain cycle (Figure 7b–d). After the 40th cycle the Lissajous figures have the typical form of a strain-hardening pattern; i.e., the stress increases with increasing strain near the extremum of the stress–strain curve. The details will be discussed in the next section.

3.3. SAXS Results under Oscillatory Shear at the First Cycle. Figures 8a and 9a show 2D SAXS patterns from the specimen sheared at 95 and 158 °C, respectively, which were taken at four representative strain phases of 0, $\pi/4$, $\pi/2$, and $3\pi/4$ rad; shear strain at those phases is illustrated in part b. These SAXS patterns were taken in the first cycle of oscillatory shear deformation. Exposure time required for the data acquisition of the 2D SAXS pattern was 1 s, which corresponds to the phase interval of 0.0944 rad ($= 2\pi \times 1.5\%$). The inner arrow at q_m indicates the scattering from {110} planes of a bcc lattice, and the outer arrow at $q_{m,p}$ indicates the scattering from isolated spheres. At 95 °C, as seen in Figure 8a, the two spots of (110) along the Y-axis (the spots along the line a) are almost stationary with the strain phase, staying parallel to the Y-axis, but other two spots of $(\bar{1}10)$ along X-axis (the spots along the line b) are oscillating around the equator with a magnitude larger than other four spots at oblique angles μ. The positions of the two spots of $(\bar{1}10)$ along X-axis (line b) are approximately at azimuthal angles 0°, −20°, 0°, and 20° with respect to the X-axis at phases 0, $\pi/2$, π, and $3\pi/2$, respectively. The SAXS intensity at $q_{m,p}$ also depends on the strain phases. It shows isotropic patterns at the minimum strain ($\gamma = 0$ at strain phases 0 and π), while the pattern deforms into ellipse most extensively at the maximum strain amplitude $\gamma = \pm 0.41$ (at strain phases $\pi/2$ and $3\pi/2$). Parts c and d of Figure 8 respectively represent a model showing preferred (110) and (200) orientation parallel to the XZ-plane under the shear deformation to explain the above observation on deformation of the lattices and the spheres, the details of which will be discussed in section 4.

In Figure 9a, the 2D SAXS pattern at 158 °C shows concentric circles at strain phases 0 and π rad, where the imposed strain is minimum. However, at strain phases $\pi/2$ and $3\pi/2$ rad, at the maximum strain ($\gamma = \pm 0.41$), both the diffraction patterns from {110} lattice planes and isolated spheres deform into elliptic shapes. These results indicate that the bcc lattice and spheres deform synchronously with the oscillatory shear deformation. Discussion on the lattice and the sphere deformation will be given later in full detail.

3.4. SAXS Results Measured at the Maximum Strain (0.41) in the 1st, the 5th, and the 40th Cycles. Figures 10 and 11 show respectively SAXS patterns at temperatures 95 and 158 °C in (a) the 1st, (b) the 5th, and (c) the 40th strain cycles measured at a particular strain phase ($\pi/2$) where the strain attains a maximum value (0.41). The exposure time for each

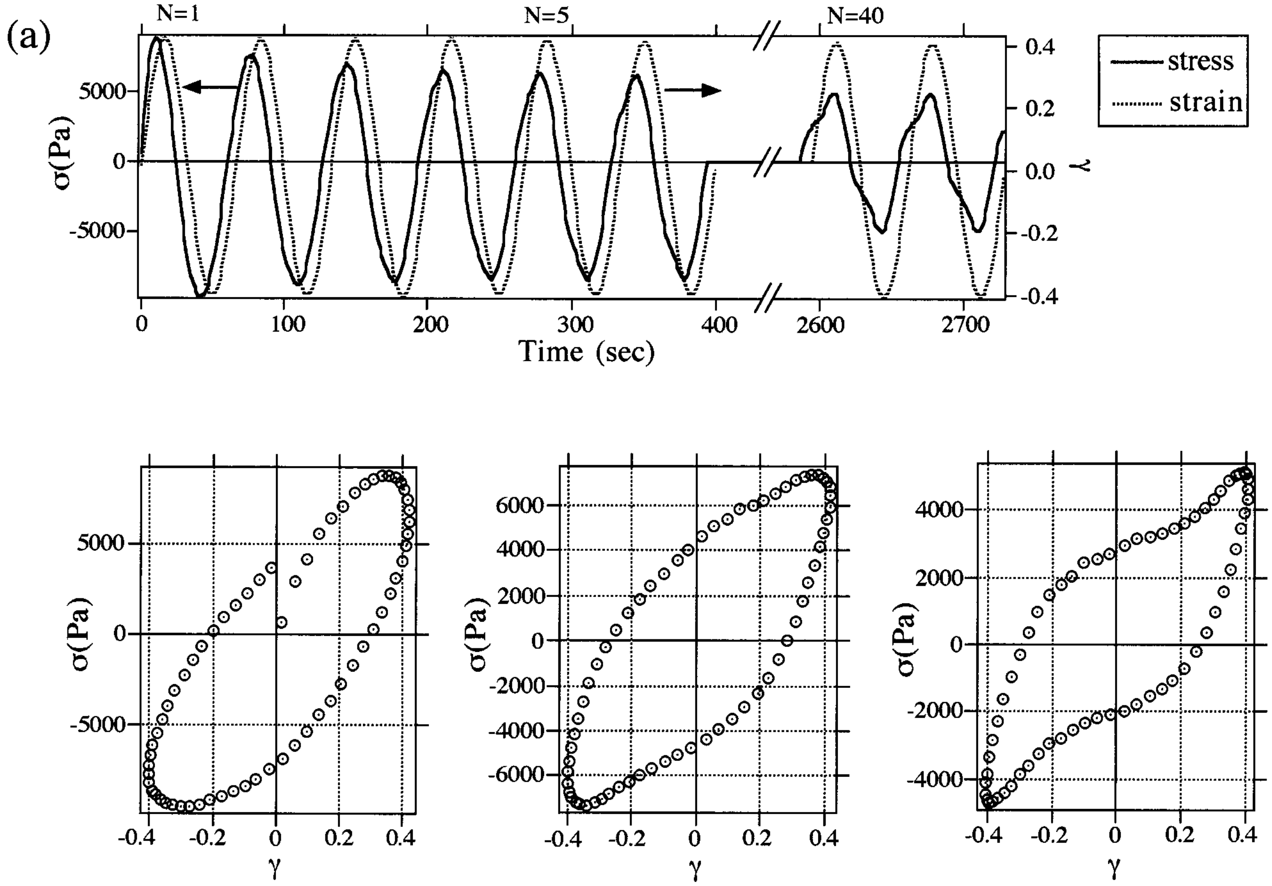

(b)1st cycle (c)5th cycle (d)40th cycle

Figure 7. Shear stress and shear strain against time detected simultaneously with the SAXS data at 158 °C (a). The Lissajous figures of shear stress versus shear strain obtained at the 1st (b), the 5th (c), and the 40th cycles (d).

2D SAXS pattern was also 1 s. Figure 10 shows the scattering patterns of the {110} plane of the bcc lattice and the isolated sphere at the maximum shear strain. The positions of those eight spots are almost constant independent of the strain cycle.

On the other hand, at 158 °C, the deformation of the scattering patterns from {110} and from isolated spheres becomes smaller as the strain cycle increases (Figure 11). The scattering pattern at the 40th cycle shows almost undeformed concentric circles.

4. Discussion

4.1. Response of Bcc Lattice and Spheres at 95 °C. As shown in Figure 8a, in the first cycle of oscillatory shear strain at 95 °C, the meridional two spots (along line a), belonging to the first-order scattering maximum at $q = q_m$ and arising from the (110) plane oriented parallel to the XZ-plane (shown in Figure 8c), are almost stationary, while the equatorial two spots (along line b), which arises from the $(\bar{1}10)$ plane (also shown in Figure 8c), oscillates about the equator with strain phase. The change of the four diffraction spots with respect to strain phase may well be explained by using a shear deformation model of a bcc lattice which involves the stationary orientation of the (110) planes parallel to XZ-plane and the rotational oscillation of the $(\bar{1}10)$ plane around Z-axis, as shown in Figure 8c. Furthermore, the rotational oscillation of other four oblique spots shown in Figure 8a also existing at around the same q_m can be ascribed to the orientational change of the (110) and $(\bar{1}10)$ planes around Z-axis as a result of the shear deformation of the lattice with its (200) planes fixed parallel to the XZ-plane during shear, as illustrated in Figure 8d. Consequently, the eight spots from the {110} diffraction as well as those from the {200} diffraction and their responses to the deformation may be attributable to the coexistence of the preferred (110) and (200) orientations of the bcc lattice, both parallel to the XZ-plane, and their deformation as illustrated in Figure 8c,d.

In response to the applied shear deformation, the bcc lattice undergoes dynamic shear deformation. An interesting point is that at the strain phase of 0 and π rad, where the magnitude of the shear strain is zero, the eight-point patterns are almost identical, and both are symmetric with respect to both the X- and Y-axes. In addition, the pattern at the strain phase of $\pi/2$ rad and the pattern at $3\pi/2$ rad are almost mirror images with respect to the Y-axis, indicating that the lattice deformation is approximately in-phase with the applied strain. In the same way, the spheres undergo dynamic shear deformation. The scattering pattern from isolated spheres shows a similar behavior as the eight-point lattice diffraction discussed above in the sense that at 0 and π rad, where the magnitude of the shear strain is zero, the scattering patterns are almost identical, and both are circulary symmetric around the incident beam axis (Z-axis), and the patterns at $\pi/2$ rad and $3\pi/2$ rad are skewed and are in mirror images with respect to the Y-axis, indicating that the deformation of the

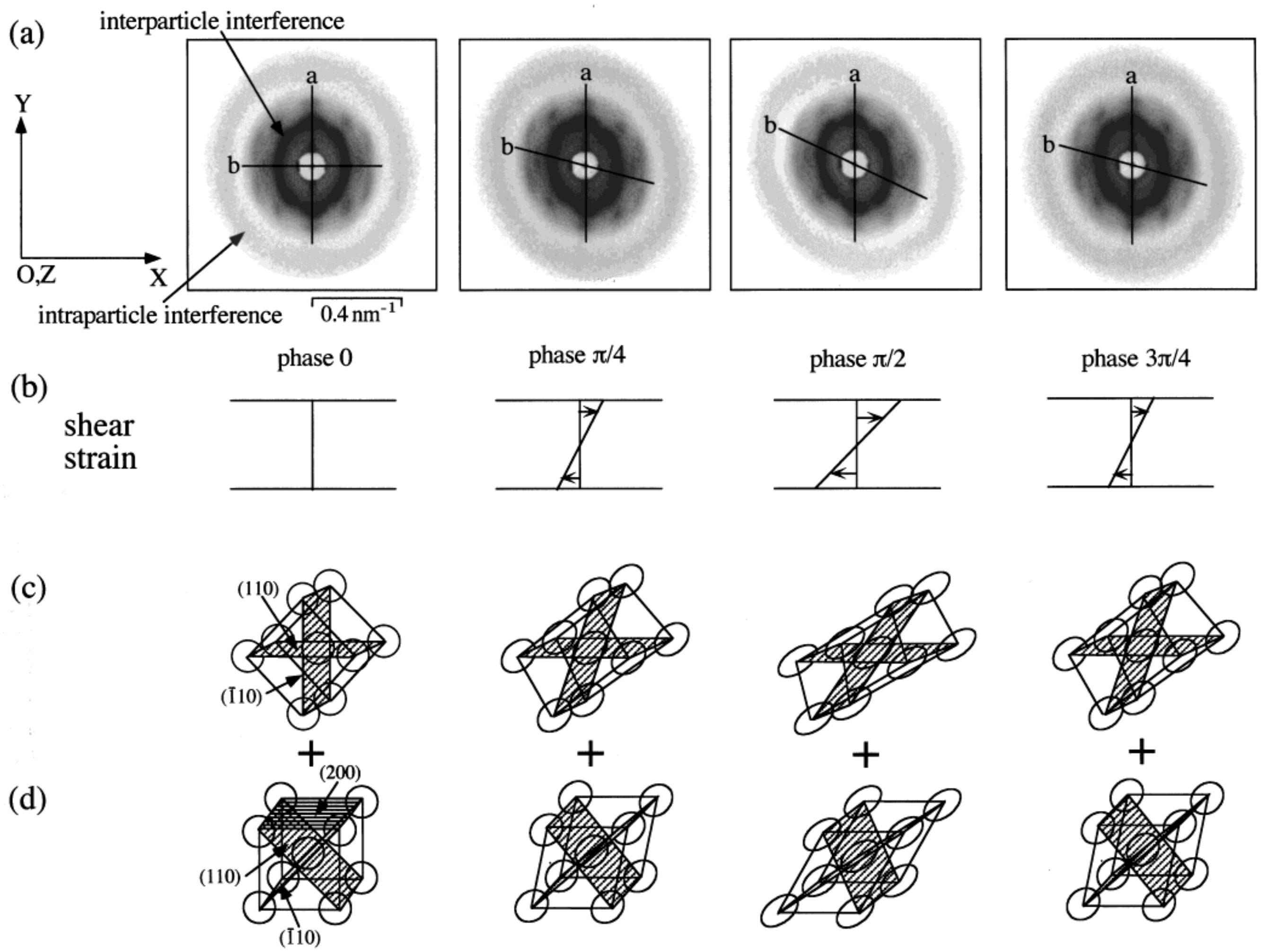

Figure 8. SAXS patterns obtained at four representative strain phases, 0, $\pi/4$, $\pi/2$, and $3\pi/4$ at the first strain cycle at 95 °C. The shear strain at each strain phase is schematized in (b). The orientation and deformation model of the lattice to explain the eight diffraction spots is shown in (c) and (d).

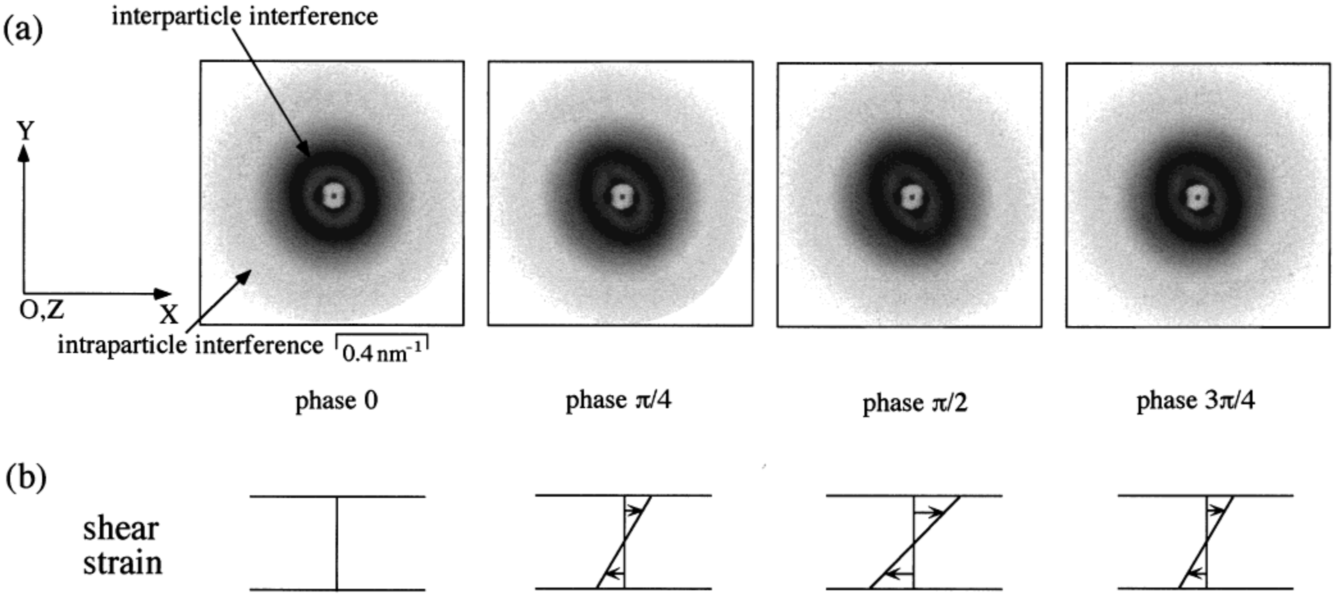

Figure 9. SAXS patterns obtained at four strain phases, 0, $\pi/4$, $\pi/2$, and $3\pi/4$ at the first strain cycle at 158 °C. The shear strain at each strain phase is schematized in (b).

spheres is also approximately in-phase with the applied strain. The microscopic deformation is well correlated to the macroscopic deformation, revealing that the both strains lag behind the stress phase. This result is consistent with the bulk mechanical behavior shown in Figure 6 and discussed in section 3.2.

4.2. Evaluations of Microscopic Strains Imposed on Lattice (γ_{lattice}) and Spheres (γ_{sphere}) at 95 °C.

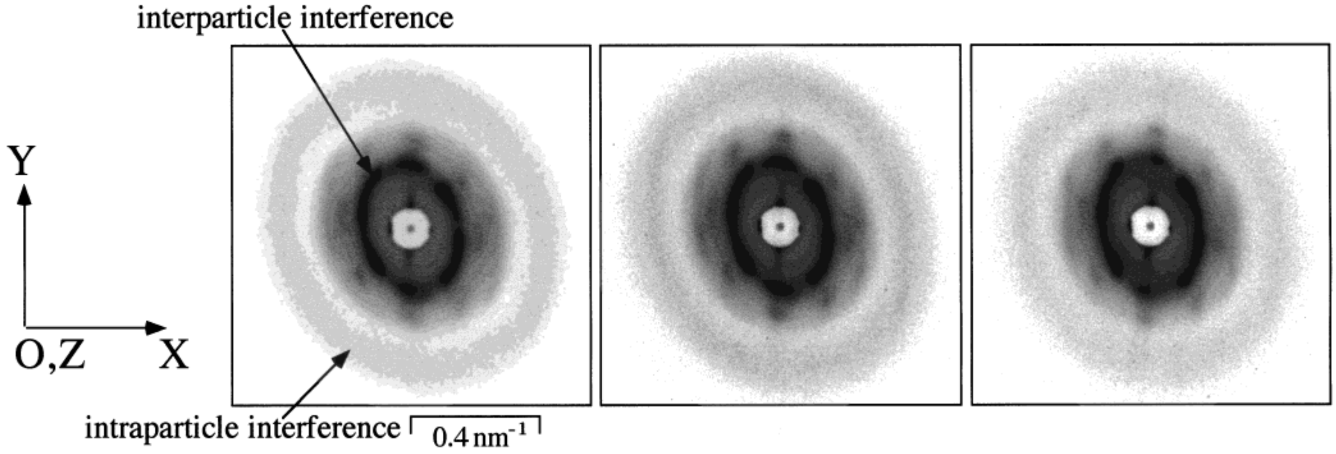

(a)1st cycle (b)5th cycle (c)40th cycle

Figure 10. SAXS patterns at (a) the 1st, (b) the 5th, and (c) the 40th cycles measured at the maximum strain, i.e., the strain phase of $\pi/2$ rad, at 95 °C.

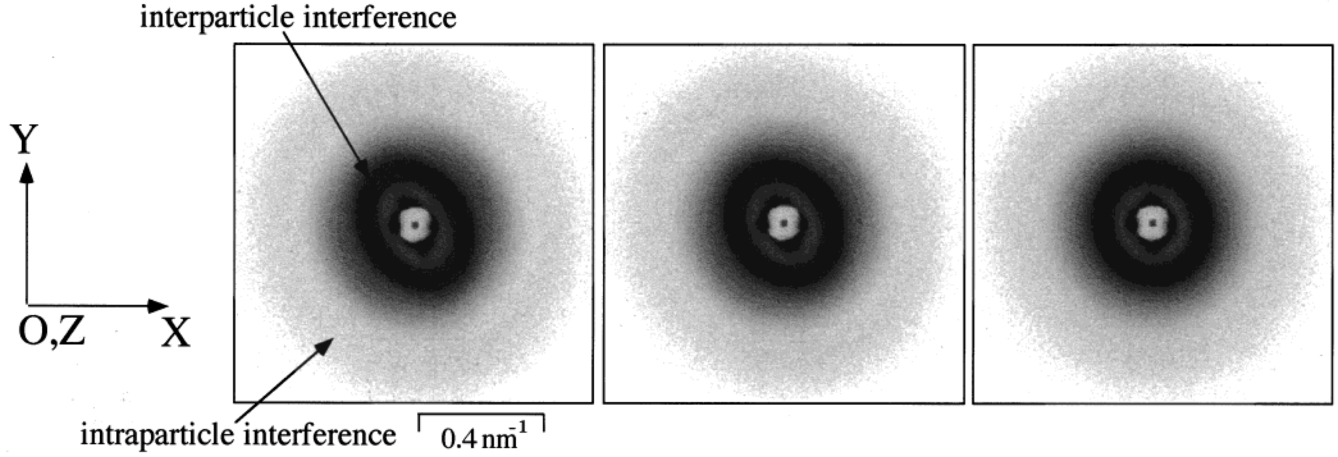

(a)1st cycle (b)5th cycle (c)40th cycle

Figure 11. SAXS patterns of (a) the 1st, (b) the 5th, and (c) the 40th cycles measured at the maximum strain at 158 °C.

Before discussing γ_{lattice} and γ_{sphere} at 95 °C, it may be useful to note a limitation or a basic assumption underlying our discussions in this section and in the preceding section in conjunction with the deformation model shown in Figure 8c,d. Generally in the volume irradiated by the incident X-ray beam there are many grains within which the bcc lattice has a coherent orientation and hence is subjected to a more or less uniform deformation. Among the grains, a part of the grains contribute to the 2D diffraction patterns in Figure 2a or 8a (the grains in diffraction conditions), but the others do not contribute to the 2D patterns (the grains in off-diffraction conditions).

Let us consider the patterns under oscillatory shear deformation at the strain phase $\phi = 0$ and $\pi/4$ in Figure 8a. We must note the following two cases reflecting the pattern change with ϕ. There are many grains which are in diffraction conditions both at $\phi = 0$ and $\pi/4$ (case A). This is the case we assumed for the deformation model shown in Figure 8c,d in the preceding section. In this case the pattern change with ϕ directly and exactly is related to the average deformation behavior of the grains in the diffraction condition. There is another case designated case B: Some grains in diffraction conditions at $\phi = 0$ (as shown in Figure 8c at $\phi = 0$) go into off-diffraction conditions at $\phi = \pi/4$, but other grains in off-diffraction conditions at $\phi = 0$ go into diffraction conditions at $\phi = \pi/4$ (as shown in Figure 8c at $= \pi/4$), giving rise to the change in diffraction pattern with ϕ that is essentially same as that in case A. In case B the pattern change with ϕ shown in Figure 8a does not represent the deformation behavior of the same grains, which casts doubt on the deformation model shown in Figure 8c and the analysis to be discussed below. Here in this work we assume that the change in the diffraction pattern with ϕ represents, at least qualitatively, an average deformation behavior of bcc in the systems. In the present SAXS work we cannot distinguish case A and case B. The distinction may be possible by evaluating the cross-correlation of time variations of intensity of different diffraction spots from {110} planes with ϕ. There will be no such problem as

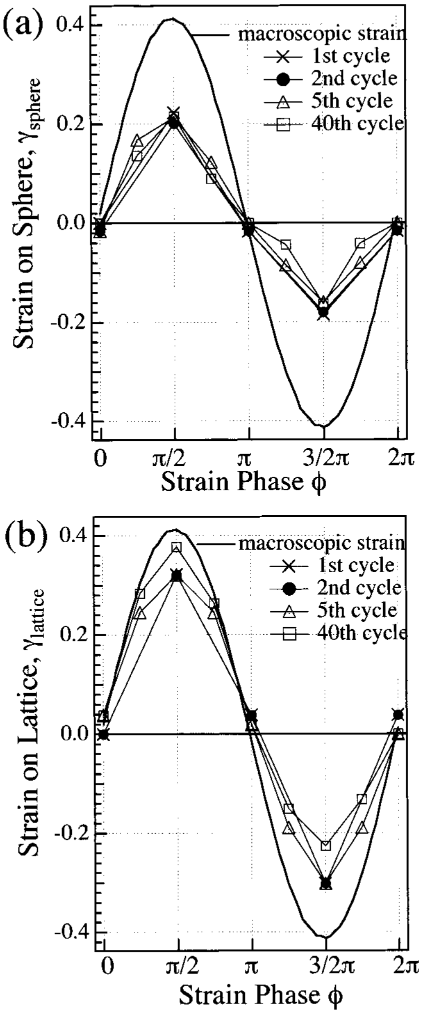

Figure 12. Local strain imposed on the sphere, γ_{sphere} (a), and on the lattice, $\gamma_{lattice}$ (b), at the 1st, the 2nd, the 5th, and the 40th cycles and at 95 °C plotted against the strain phase.

described above in evaluating the microscopic strain imposed on the spheres: The change in the scattering ring from the sphere form factor always represents the average deformation of the spheres.

The average local shear strains on the spheres, γ_{sphere}, and the lattice, $\gamma_{lattice}$, were calculated as a function of strain phase from the phase-resolved SAXS patterns on the basis of the affine deformation as detailed in Appendix. These results were obtained for the measurement at 95 °C and at various strain cycles N, $N = 1$, 2, 5, and 40. Figure 12a shows γ_{sphere} calculated from the deformation of the scattering pattern from the isolated spheres, and Figure 12b shows $\gamma_{lattice}$ calculated from the shift of the equatorial two point pattern from *OX* direction along the azimuthal angle, which arises from the $(\bar{1}10)$ plane orientation as shown in Figure 8c. A comparison of γ_{sphere}, $\gamma_{lattice}$, and the macroscopic strain (γ_{macro}) plotted as a function of the strain phase in Figure 12 clearly shows that the sphere and the lattice deformation occur in phase with γ_{macro}.

As seen in Figure 12b, $\gamma_{lattice}$ is ~70% of γ_{macro} and shows no appreciable change up to the 40th strain cycle, which means that the lattice is deforming almost affinely and in phase with the macroscopic deformation under this experimental condition. Correspondingly, the macroscopic stress level did not change significantly with N as shown in Figure 6a. The loss of the local strain by 30% may be attributed to an excess local strain (γ_{defect}) concentrated at the grain boundaries or some localized defect regions. It is interesting to note that γ_{defect} itself increases and decreases synchronously with γ_{macro} as $\gamma_{lattice}$ is almost independent of N. The small amount of the stress decay shown in Figure 6a may be related to the localized deformation in the defects. The $\gamma_{lattice}$ at the 40th strain cycle seems to be somewhat shifted to the positive direction by an unexplainable reason, though the shift is not significant.

On the other hand, γ_{sphere} is ~50% and remains almost constant up to the 40th strain cycle (Figure 12a). It should be pointed out that the spheres deform to a less extent than the lattice, though the sphere is mechanically softer than the matrix. Increase in the free energy of a spherical microdomain upon deformation is composed of (a) the elastic free energy associated with deformation of the short PEP block chains comprising the spheres and (b) the free energy associated with interfacial deformation. In the strong segregation state, these two contributions may be sufficiently large compared with the free energy of the lattice deformation which involves deformation of PS corona chains emanating from the sphere interfaces, resulting in less deformation of spherical domains than the matrix.

The eight spots from {110} already existed before the application of shear did not change with N. Moreover, a sharpening of spots along the azimuthal angle μ was not observed even after the application of a number of shear cycles (as seen in Figure 10). The important point to note is that under this condition the shear deformation did not induce or promote a preferential orientation of the lattice plane. It is a big contrast to the results reported by Almdal et al.[14] and Okamoto et al.,[16] who reported the shear-induced preferential orientation of the particular lattice plane.

4.3. Response of Bcc Lattice and Spheres at 158 °C. The 2D SAXS pattern obtained at 158 °C exhibits no azimuthal angle dependence before the application of the shear deformation (Figure 3a), which indicates that a preferential orientation existed in the specimen at lower temperature 95 °C was relaxed upon raising temperature to 158 °C.

Upon imposing an oscillatory shear deformation, both the scattering ring of the bcc {110} plane and that from the isolated particle deform at the first cycle as shown in Figure 9a, indicating that both the bcc lattice and the spheres undergo a dynamic shear deformation. It was observed in the preceding section that the shear deformation at 95 °C did not involve a preferential lattice orientation. We would like to emphasize that the shear deformation does not involve a preferential orientation at 158 °C also, as clearly seen in Figure 11. We may, therefore, reasonably conclude that the harder spheres in the soft matrix (as in the case of Okamoto et al.[16]) or at least equal stiffness of the matrix and sphere phases (as in the case of Almdal et al.[14]) is one of the important factors for the preferential orientation under LAOS.

4.4. Evaluations of $\gamma_{lattice}$ and γ_{sphere} at 158 °C. Upon analyzing the scattering patterns in the same manner as discussed in the preceding section, it is concluded that both $\gamma_{lattice}$ and γ_{sphere} are approximately in-phase with γ_{macro} at 158 °C also, as shown in parts a and b of Figure 13, respectively, at various shear cycles N, $N = 1$, 5, and 40. This means that the microscopic deformation on the spheres and lattices lags in phase with the macroscopic stress.

The analysis of the γ_{lattice} at 158 °C is again based on the same assumption as that discussed in section 4.2. At 158 °C, the system composed of very many small grains so that many grains in diffraction conditions for the {110} planes give a continuous diffraction ring as shown in Figures 3, 9, and 11. We assume that the change in the shape of the diffraction ring with strain phase ϕ and strain cycle N is related to average deformation of {110} lattice spacing and hence to average local strain γ_{lattice} imposed on the {110} lattice spacing.

At 158 °C, γ_{lattice} remains ~40% of γ_{macro} until the 5th strain cycle and then drastically decreases to 10% at the 40th cycle, which means that a fundamental change in the deformation mechanism occurred between the 5th cycle and the 40th cycle. On the other hand, γ_{sphere} is 20% at the first cycle, 12% at the 5th cycle, and 8% at the 40th cycle. At the 40th cycle both γ_{lattice} and γ_{sphere} become less than 10% of γ_{macro}. It seems reasonable to state that most of the deformation takes place at the defective regions or the grain boundary regions and γ_{defect} increases with N on the contrary to the case at 95 °C.

We are unable to discuss the effect of the localized deformation at the defects based only on the SAXS results, because our SAXS results show the effect only indirectly through γ_{lattice} and γ_{sphere}. Consequently, the clarification of the effect is left unsolved until a close examination of the effect will become possible using other methods that enable us to directly explore the grain boundary deformation or deformation in the localized defect area. It is intriguing to note that a ratio of $\gamma_{\text{sphere}}/\gamma_{\text{lattice}}$ increases with N, i.e., $^1/_3$, $^2/_9$, and $^4/_5$ for $N = 1$, 5, and 40, respectively, at 158 °C, whereas the ratio remains constant independent of N, equal to $^5/_8$ at 95 °C. If we compare the ratio at $\gamma_{\text{sphere}}/\gamma_{\text{lattice}}$ at $N = 40$ and at 95 °C and that at $N = 40$ and at 158 °C, the latter is larger; viz., the spheres tend to be deformed as easily as the lattice at 158 °C.

4.5. Analysis of the Mechanical Response. Macroscopic stress and strain measured simultaneously with 2D-SAXS patterns at temperatures 95 and 158 °C are plotted against time in Figures 6a and 7a, respectively, showing that the stress amplitude decayed with strain cycle N at both temperatures. As seen Figure 6b–d and Figure 7b–d, the Lissajous figures obtained at the first cycle approximately show a linear stress response at both temperatures, but the nonlinearity generally develops and increases with N. The degree of nonlinearity at 158 °C is apparently larger than that at 95 °C. In particular, the Lissajous figure at 158 °C in the 40th cycle shows a pattern typical of strain hardening.

At $N = 40$ where the strain hardening is remarkable, γ_{lattice} and γ_{sphere} are quite small compared with γ_{macro}. Since a major fraction of γ_{macro} should be taken by γ_{defect}, the deformation of the defect regions should be responsible for the strain-hardening effect.

To analyze the nonlinearity of stress response in a more quantitative way, we expand the stress to the Fourier series, defined by

$$\sigma(t) = \sum_k (\sigma'_k + i\sigma''_k) \exp(ik\omega t), \quad k = 1, 2, 3, ... \qquad (1)$$

Figures 14 and 15 show the absolute values of first-, third-, and fifth-order Fourier components of the stress as a function of strain cycles at 95 and 158 °C, respectively. The absolute value of kth order Fourier

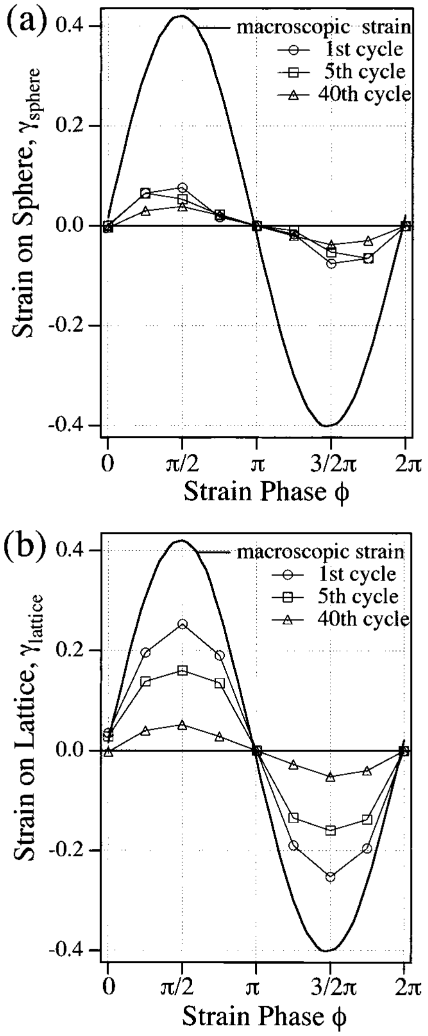

Figure 13. Local strain imposed on the sphere, γ_{sphere} (a), and on the lattice, γ_{lattice} (b), at the 1st, the 2nd, the 5th, and the 40th cycles and at 158 °C plotted against the strain phase.

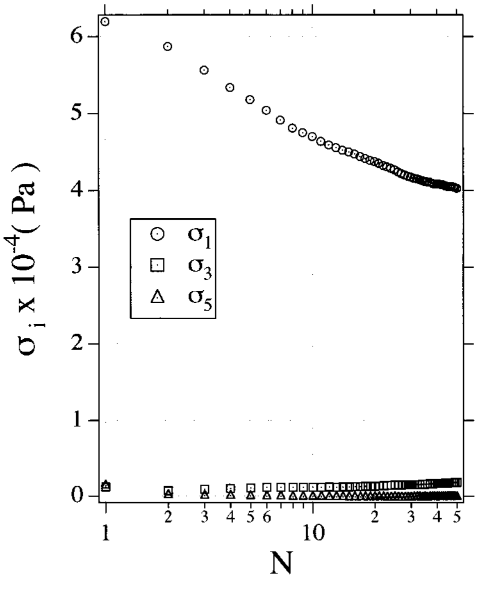

Figure 14. Absolute values of the 1st, the 3rd, and the 5th order Fourier coefficients of shear stress plotted against the strain cycle N at 95 °C.

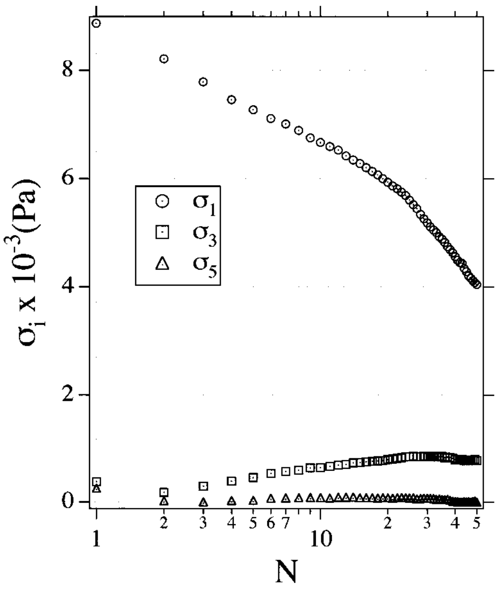

Figure 15. Absolute values of the 1st, the 3rd, and the 5th order Fourier coefficients of shear stress plotted against the strain cycle *N* at 158 °C.

component of the stress, σ_k, is defined by

$$\sigma_k = |\sigma_k{}^*| = \sqrt{(\sigma_k')^2 + (\sigma_k'')^2} \qquad (2)$$

where

$$\sigma_k{}^* = \sigma_k' + i\sigma_k'', \quad k = 1, 2, 3, ... \qquad (3)$$

As seen in Figures 14 and 15, the third-order component is much larger than the fifth-order component at all cycles at both temperatures. And higher-order components than the fifth order, though not shown in the figures, are less than the fifth component. We note that in Figure 14 the third- and fifth-order components are much smaller than the first-order component, which indicates that the stress response is relatively linear at 95 °C. On the contrary, as seen in Figure 15, a relative contribution of the third-order component to the first-order component at 158 °C is much larger than that at 95 °C, and it becomes large with strain cycle *N* at 158 °C, which indicates that the nonlinearity of the stress is large and grows with increasing strain cycles under LAOS at 158 °C.

Comparing this mechanical behavior with the SAXS results gives us the following conclusions. (i) At 95 °C the PEP spheres and the lattice deform in-phase with the applied strain at all cycles, with γ_{sphere} and γ_{lattice} as high as 50% and 75% of γ_{macro}, respectively. The stress response shows a relatively linear response, and the stress does not decay significantly with *N*. (ii) At 158 °C the spheres and the lattice deform only 20% and 40% of γ_{macro} at the first cycle of the application of the oscillatory shear deformation, but γ_{sphere} and γ_{lattice} decrease with *N*, in parallel to the growth of the nonlinearity of the stress response. To put it another way, when the stress response is linear, the sphere and the lattice deform to a greater extent, and the localized deformation of the defects does not contribute significantly to the macroscopic strain. On the other hand, when the stress response is nonlinear, the sphere and the lattice deform less. The nonlinear behaviors and the strain hardening behaviors may be related to the excess local deformation in the defective region or in the grain boundary region.

Doi et al.[34] presented a theory for analyzing anomalous rheological behavior of the ordered cylindrical mesophase of block copolymers. Their approach is based on a coupled multilayer model; therefore, it may be essentially applicable to the bcc mesophase as well. They obtained a Lissajous pattern showing the strain-hardening phenomenon when both strain amplitude and frequency are high. The computer simulations[34] show that the onset of an instability in terms of the slippage between layers at the high strain amplitudes and frequencies makes the layers separate into two groups, resulting in the strain-hardening Lissajous pattern.[34] In light of their analysis, the change of our Lissajous pattern from the linear response to the strain-hardening one with increasing *N* at 158 °C (Figure 7) may indicate a growth of the instability in the slippage between layers with *N*. The growth should then be expected to reduce γ_{lattice} and γ_{sphere}.

5. Concluding Remarks

In this work we presented the deformation mechanism of the SEP block copolymer system with the bcc mesophase composed of PEP spherical microdomains in the PS matrix under LAOS at 95 °C, which is a little higher than the glass transition temperature of the matrix polystyrene phase (T_g), and at 158 °C, which is high enough compared with the T_g of the PS phase. At both temperatures the spheres are much softer than the matrix. Further, these temperatures are far below the ODT temperature T_{ODT}, so that the system is in a strong segregation regime. These experimental conditions are very different from those previously reported by Almdal et al.[14] and Okamoto et al.[16] Almdal et al. reported the case where both PEP sphere and PEE matrix are soft at temperatures relatively close to T_{ODT}, so that the segregation power between the two blocks are not strong, whereas Okamoto et al. reported the case where the vitrified and rigid PS spheres in the matrix of soft PEP matrix at temperatures far below T_{ODT} in the strong segregation.

Almdal et al. and Okamoto et al. elucidated strong preferential orientation of a particular lattice plane induced after and during LAOS, respectively, although the orientation behaviors of the two cases are quite different. On the contrary, the system studied here does not exhibit any strong preferential orientations of lattice planes during LAOS. Namely, the initial orientation of the lattices is recovered at the zero strain phase of each cycle of LAOS. The lattice tends to be deformed and oriented with increasing $|\gamma|$, but the deformation and orientation are relaxed with decreasing $|\gamma|$. Thus, the difference in the mechanical property of the matrix against that of the spheres seems to give an important factor for producing the preferential orientation of the particular lattice planes under the shear deformation. Needless to say, this difference in the mechanical properties should be taken into consideration in conjunction with the differences in strain amplitude, angular frequency, and temperature relative to T_{ODT} for the various systems studied or to be studied.

Beside the preferential orientation of the particular lattice plane with respect to the shear plane, we have reported deformation of the lattice and the spheres synchronously with strain phase at the two representative temperatures and the given angular frequency as

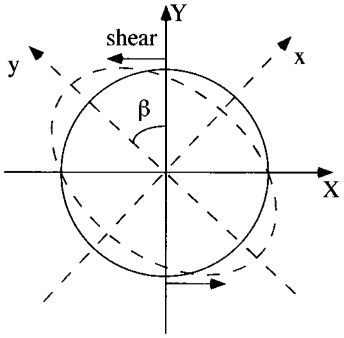

Figure 16. Model showing the undeformed sphere (thin line) and the deformed sphere (broken line) for evaluating the local shear strain on the sphere, γ_{sphere}, and the lattice, γ_{lattice}.

a function of the strain cycle N under LAOS. We reported for the first time the microscopic strain actually imposed on the lattice γ_{lattice} and that on the sphere γ_{sphere} as well as a function of the strain phase and interrelated them to the nonlinear stress response and the strain-hardening effect. We hope that information obtained here contributes to understanding of the effect of shear deformation on ordered block copolymers. More advanced experimental and theoretical investigations of the effect of domain structures on the shear orientation and deformation mechanisms as well as on the nature of the grain boundary deformation deserve future works.

Acknowledgment. This work was performed under the approval of the Photon Factory Program Advisory Committee (Proposal Nos. 95G345 and 97G245) and supported in part by a Grant-in-Aid for Scientific Research (No. 12305060) from the Ministry of Education, Science and Culture, Japan.

Appendix

Calculation of the Local Strain Imposed on the Sphere γ_{sphere} and the Lattice γ_{lattice}. Figure 16 shows the projections of undeformed and deformed spheres on the XY-plane, where the X-axis is the shear direction and the Y-axis is the velocity gradient direction. The shear strain on the sphere can be evaluated in terms of the aspect ratio of the deformed sphere. Assuming the affine deformation,

$$(X - \gamma Y)^2 = Y^2 = R_0^{\ 2} \tag{A1}$$

where γ is the shear strain and R_0 is the radius of the undeformed sphere. Assuming x- and y-axes are along the two principal axes of the deformed sphere,

$$rx^2 + r^{-1}y^2 = R_0^{\ 2} \tag{A2}$$

where r is the aspect ratio, i.e., the ratio of the major axis to the minor axis of the projection of the deformed sphere on the xy-plane. The coordinate systems Oxy and OXY have the relationship

$$x = X\cos\beta + Y\sin\beta \tag{A3}$$

$$y = -X\sin\beta + Y\cos\beta \tag{A4}$$

where β is the angle between the Y-axis and the y-axis, i.e., the major axis of the deformed sphere. Using eqs A1–A4, we obtain

$$\gamma = \sqrt{r} - \frac{1}{\sqrt{r}} \tag{A5}$$

The local strain imposed on the spheres was determined from the aspect ratio of the elliptical-ring type SAXS pattern arising from the first-order intraparticle scattering maximum (the first-order maximum from the form factor of the deformed spheres) observed in the XY-plane with an incident X-ray along the Z-axis and by using eq A5. Note that the maximum position of the elliptical ring is directionally dependent: If the maximum positions parallel to principal axes of spheroids, Ox and Oy, are defined as $q_{\text{m,p},x}$ and $q_{\text{m,p},y}$ then r is given by $r = q_{\text{m,p},x}/q_{\text{m,p},y}$.

The local strain of the lattice was also evaluated by using eq A5 and from the aspect ratio of the elliptical ring arising from the interparticle interference maximum, reflecting the diffraction maximum from the corresponding lattice plane, in the case when the orientation distribution of the lattice is rather broad and the diffraction maximum shows an elliptical ring (see Figures 9 and 11).

However, when the domains have a preferential orientation as in the patterns shown in Figures 8 and 10, the interparticle scattering shows spotlike patterns. In this situation, the local strain γ on the lattice can be evaluated from

$$\gamma = \tan\mu_{\max} \tag{A6}$$

where $\mu_{\max}$ is the angle between the X-axis and the line connecting two $(\bar{1}10)$ spots (the line b as shown in Figure 8). As seen in Figure 8, two (110) spots in the meridian are almost stationary during oscillatory shear deformation of the sample, suggesting no rotational motion of the lattice. Therefore, the orientation of the $(\bar{1}10)$ plane directly reflects the local shear strain on the lattice as illustrated in Figure 8.

References and Notes

(1) Keller, A.; Pedemonte, E.; Willmouth, F. M. *Nature* **1970**, *225*, 538.
(2) Hadziioannou, G.; Mathis, A.; Skoulious, A. *Colloid Polym. Sci.* **1979**, *257*, 136.
(3) Koppi, K. A.; Tirell, M.; Bates, F. S.; Almdal, K.; Colby, R. H. *J. Phys. II* **1992**, *2*, 1941.
(4) Winey, K. I.; Patel, S. S.; Larson, R. G.; Watanabe, H. *Macromolecules* **1993**, *26*, 2542.
(5) Winey, K. I.; Patel, S. S.; Larson, R. G.; Watanabe, H. *Macromolecules* **1993**, *26*, 4373.
(6) Okamoto, S.; Saijo, K.; Hashimoto, T. *Macromolecules* **1994**, *27*, 5547.
(7) Patel, S. S.; Larson, R. G.; Winey, K. I.; Watanabe, H. *Macromolecules* **1995**, *28*, 4313.
(8) Pinheiro, B. S.; Hajduk, D. A.; Gruner, S. M.; Winey, K. I. *Macromolecules* **1996**, *29*, 1482.
(9) Polis, D. L.; Winey, K. I. *Macromolecules* **1996**, *29*, 8180.
(10) Scott, D. B.; Waddon, A. J.; Lin, Y. G.; Karasz, F. E.; Winter, H. H. *Macromolecules* **1992**, *25*, 4175.
(11) Morrison, F. A.; Mays, J. W.; Muthukmar, M.; Nakatani, A. I.; Han, C. C. *Macromolecules* **1993**, *26*, 5271.
(12) Winter, H. H.; Scott, D. B.; Gronski, W.; Okamoto, S.; Hashimoto, T. *Macromolecules* **1993**, *26*, 7236.
(13) Jackson, C. L.; Barnes, K. A.; Morrison, F. A.; Mays, J. W.; Nakatani, A. I.; Han, C. C. *Macromolecules* **1995**, *28*, 713.
(14) Almdal, K.; Koppi, K.; Bates, F. S. *Macromolecules* **1993**, *26*, 4058.
(15) Phoon, C. L.; Higgins, J. S.; Allegra, G.; van Leeuwen, P.; Staples, P. *Proc. R. Soc. London A* **1993**, *442*, 221.
(16) Okamoto, S.; Saijo, K.; Hashimoto, T. *Macromolecules* **1994**, *27*, 3753.
(17) Koppi, K. A.; Tirrell, M.; Bates, F. S. *Phys. Rev. Lett.* **1993**, *70*, 1449.

(18) Bates, F. S.; Koppi, K. A.; Tirrell, M.; Almdal, K.; Mortensen, K. *Macromolecules* **1994**, *27*, 5934.

(19) Hamley, I. W.; Koppi, K. A.; Rosedale, J. H.; Bates, F. S.; Almdal, K.; Mortensen, K. *Macromolecules* **1993**, *26*, 5959.

(20) Koppi, K. A.; Tirrell, M.; Bates, F. S.; Almdal, K.; Mortensen, K. *J. Rheol.* **1994**, *38*, 999.

(21) Forster, S.; Khandpur, A. K.; Zhao, J.; Bates, F. S.; Hamley, I. W.; Ryan, A. J.; Bras, W. *Macromolecules* **1994**, *27*, 6922.

(22) Khandpur, A. K.; Forster, S.; Bates, F. S.; Hamley, I. W.; Ryan, A. J.; Bras, W.; Almdal, K.; Mortensen, K. *Macromolecules* **1995**, *28*, 8796.

(23) Hosemann, R.; Bagchi, S. N. *Direct Analysis of Diffraction by Matter*; North-Holland: Amsterdam, The Netherlands, 1962.

(24) Matsuoka, H.; Tanaka, H.; Hashimoto, T.; Ise, N. *Phys. Rev.* **1987**, *B36*, 1754. Matsuoka, H.; Tanaka, H.; Iizuka, N.; Hashimoto, T.; Ise, N. *Phys. Rev.* **1990**, *B41*, 3854.

(25) See for example: Shibayama, M.; Hashimoto, T.; Kawai, H. *Macromolecules* **1983**, *16*, 16.

(26) Ferry, J. D *Viscoelastic Properties of Polymers,* 3rd ed.; John Wiley and Sons: New York, 1980.

(27) Onogi, S.; Masuda, T.; Kitagawa, K. *Macromolecules* **1970**, *3*, 109.

(28) Suehiro, S.; Saijo, K.; Seto, T.; Sakamoto, N.; Hashimoto, T.; Ito, K.; Amemiya, Y. *J. Synchrotron Radiat.* **1996**, *3*, 225.

(29) Hashimoto, T.; Suehiro, S.; Shibayama, M.; Saijo, K.; Kawai, H. *Polym. J.* **1981**, *13*, 501. Hashimoto, T.; Saijo, K.; Kosc, M.; Kawai, H.; Wasiak, A.; Ziabicki, A. *Macromolecules* **1985**, *18*, 472.

(30) Suehiro, S.; Saijo, K.; Ohta, Y.; Hashimoto, T.; Kawai, H. *Anal. Chim. Acta* **1986**, *189*, 41.

(31) Hashimoto, T.; Okamoto, S.; Saijo, K.; Kimishima, K.; Kume, T. *Acta Polym.* **1995**, *46*, 463.

(32) Rubinstein, M.; Obukhov, S. P. *Macromolecules* **1993**, *26*, 1740.

(33) The form factor of a spheroid is given as $\Phi(U) = (3/U^2)(\sin U - U \cos U)$, where $U = U_0\{1 + (r^2 - 1) \cos^2 \mu\}^{1/2}$ for small-angle scattering, $U_0 = qR_{OX}$, r is the aspect ratio ($=R_{OY}/R_{OX}$), μ is the angle between the scattering vector and the Y-axis. Here R_{OX} and R_{OY} are radii of the spheroid along X- and Y-axes, respectively. As $U_{OX} = U(\mu{=}0) = rU_0 = qR_{OX}$, and $U_{OY} = U(\mu{=}\pi/2) = U_0 = qR_{OY}$, and $U = 5.765$ at the first-order maximum from the form factor, R_{OX} and R_{OY} are calculated as $5.765/q_{\mathrm{m,p},OX}$ and $5.765/q_{\mathrm{m,p},OY}$, respectively. The definition of $q_{\mathrm{m,p},OY}$ and $q_{\mathrm{m,p},OX}$ is given in the text.

(34) Doi, M.; Harden, J. L.; Ohta, T. *Macromolecules* **1993**, *26*, 4935.

MA000226M